

¹ Shape optimization for improved
² understanding of magmatic plumbing
³ systems

⁴ **Théo Perrot, Freysteinn Sigmundsson**
⁵ June 2024

⁶ **Abstract**

⁷ In volcano geodesy, inverse problems caused by identifying the location and
⁸ shape of magmatic bodies based on ground deformation data are common.
⁹ Traditional approaches often rely on models with predefined shapes, which
¹⁰ can limit their accuracy. To address this, we present a shape optimisa-
¹¹ tion method using a level-set approach that flexibly determines the optimal
¹² shape of a magma chamber without prior shape assumptions. By minimis-
¹³ ing the discrepancy between observed and modelled surface displacements,
¹⁴ our adapted algorithm becomes suitable for solving inverse volcano deforma-
¹⁵ tion problems. We explore the capabilities of this approach with synthetic
¹⁶ data and apply it to InSAR observations of the Svartsengi volcanic system in
¹⁷ Iceland, demonstrating its potential to improve volcanic hazard assessment
¹⁸ after maturation through future work.

19 **1 Introduction**

20 **1.1 Challenge**

21 In volcano geodesy, inverse problems are central to estimating the position
22 of magmatic bodies using ground motion as a proxy. Displacement is ob-
23 served by geodetic measurements such as Global Navigation Satellite System
24 (GNSS) point positioning, leveling campaigns, or Synthetic Aperture Radar
25 (InSAR) interferometry within a volcanic field, and the subsurface processes
26 causing the movement are inferred from these observations (Dzurisin, 2007).
27 Magmatic sources are modeled as pressurized cavities that deform the sur-
28 rounding host rocks and cause the surface to move. Various inversion meth-
29 ods based on parametric analytical or numerical models aim at finding the
30 optimal values for the vector of d free parameters $\vec{m} \in \mathbb{R}^d$ of the model. Then
31 an error function $J(\vec{m})$ is representative of the misfit between the observed
32 displacements and the prediction of the model. \vec{m}_{opt} can then be found using
33 various inversion techniques that minimize J : global optimization based on
34 analytic (Cervelli et al., 2001) or numerical models (Hickey and Gottsmann,
35 2014, Charco and Galán del Sastre, 2014), Bayesian inference (Bagnardi and
36 Hooper, 2018, Trasatti, 2022), or genetic algorithms (Velez et al., 2011) on
37 analytic models. The choice of the method is constrained by the reasonable
38 number of evaluations of $J(\vec{m})$: numerical models handle a complex descrip-
39 tion of the system, but are computationally expensive compared to analytic
40 models, which on the other hand may lead to an oversimplification (Taylor
41 et al., 2021).

42 However, each of these finite-dimensional optimization methods is limited
43 by the intrinsic assumption of a definite parametric shape for the source. In
44 fact, analytic expressions can be derived for only a few regular shapes such as
45 point source (Mogi, 1958), finite sphere source (McTigue, 1987), or ellipsoidal
46 source (Yang et al., 1988), and any numerically generated shape must be
47 parameterized to be inverted. Even in the case where complex shapes are
48 chosen, they would require additional describing parameters, and ultimately
49 any of the above methods may face the curse of dimensionality. The goal of
50 this paper is not to give a definitive answer to these limitations, but rather
51 to lay the first stone for a new approach that overcomes these difficulties.

52 **1.2 Shape optimization**

53 Shape (and topology) optimization aims to find the shape that minimizes
54 a given function defined on a given system, without the need for prior as-
55 sumptions about shape and topology. It is actively developed by part of the

56 applied mathematics community and is widely used in engineering to find op-
57 timal designs for systems: In structural mechanics, to maximize the stiffness
58 of a solid structure such as a cantilever beam (Bendsøe and Sigmund, 2004),
59 in fluid-structure interaction on heat exchangers or flying obstacles (Fep-
60 pon et al., 2020), and even as a way to explore new architecture for buildings
61 (Beghini et al., 2014). Most finite element simulation and design software now
62 implements an embedded shape optimization module (Frei, 2015, Slavov and
63 Konsulova-Bakalova, 2019, Le Quilliec, 2014). However, its use has not yet
64 been reported in the context of inverse problems in volcano geodesy, where
65 it can overcome the shape hypothesis problem as long as an internal pressure
66 value is assumed.

67 Many paradigms coexist in shape optimization as reviewed by Sigmund
68 and Maute, 2013, one of the most popular being SIMP optimization, where a
69 density value is optimized for each element of the mesh with values between
70 0 (void) and 1 (material) before being black and white filtered to output
71 a design (Sigmund, 2001,Bendsøe and Sigmund, 2004), with several open
72 source implementations (Andreassen et al., 2011,Hunter et al., 2017). We
73 chose level-set shape optimization instead because it has the advantage of
74 providing an explicit representation of the boundary at each step of the op-
75 timization, which is crucial for us as explained later (section 2). For this, we
76 relied on the work of Dapogny and Feppon, 2023, who thoroughly described
77 and vulgarized the method, as well as providing a freely available open source
78 implementation of the method, **sotuto**(Dapogny and Feppon, 2022, Octo-
79 ber 4/2024), which we modified and extended to adapt it to inverse geodetic
80 problems.

81 2 Method

82 Here we briefly present the key ingredients of level set shape optimization
83 along with their implications for our problem. The full mathematical back-
84 ground on which it relies is not detailed, but see this chapter by Allaire et al.,
85 2021 for a comprehensive step-by-step description supported by proofs and
86 theorems. It is also worth noting that many aspects of secondary importance
87 to the method are not mentioned for the sake of brevity. For the unfamiliar
88 reader interested in understanding the method, the lecture (especially part
89 III) given by Dapogny and Bonnetier, n.d. at the Université Grenoble Alpes
90 is also recommended.

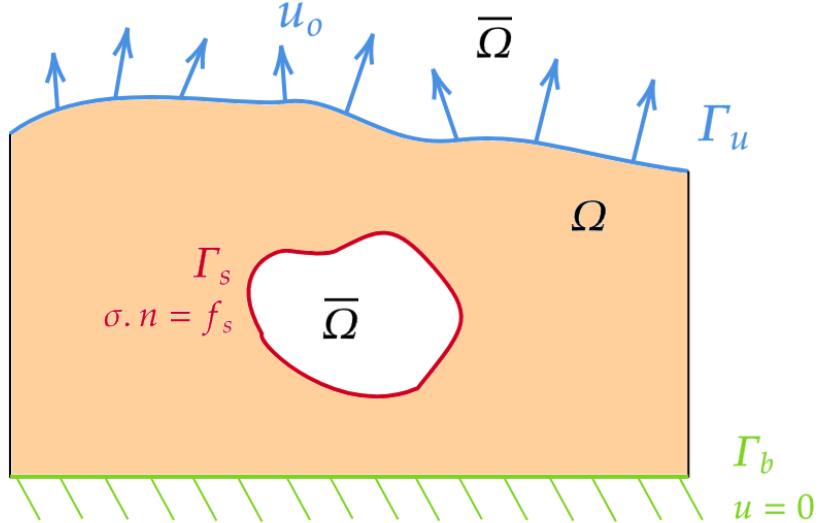


Figure 1: 2D sketch of the problem. The optimized boundary (where the level-set function is zero) is the magma chamber wall Γ_s subjected to a uniform normal load $\sigma(u).n = f_s$ on Γ_s , where $f_s = -\Delta P.n$, where n is the unit normal vector and ΔP is the pressure change between the magma source and the surrounding crust. The bottom surface Γ_b is fixed ($u = 0$). The other boundaries are free. The target displacement field u_o is known on the upper surface Γ_u .

91 2.1 Model

92 Let Ω be a bounded domain of \mathbb{R}^3 whose shape we want to optimize by
 93 modifying parts of its boundary $\partial\Omega$. As for classical analytical models of
 94 volcanic deformation induced by magmatic activity, Ω is a domain represent-
 95 ing a portion of the shallow Earth crust, including the volcano, assumed
 96 to be homogeneous, isotropic, and elastic. The governing equations are
 97 $-\text{div}(Ae(u)) = 0$ in Ω , where $e(u)$ is the strain tensor of the displacement
 98 field u and A is the constitutive law tensor, $Ae = 2\mu e + \lambda \text{tr}(e)\text{Id}$ for linear
 99 elasticity. Boundaries under different conditions, see Fig. 1 for all notations.

100 The part of $\partial\Omega$ to be optimized is Γ_s , the boundary magma chamber,
 101 which is modeled as an empty, uniformly pressurized cavity. Therefore, a
 102 value for the internal pressure ΔP must be assumed (see Discussion for devel-
 103 opment). In the following text we talk about optimizing $\partial\Omega$, but in practice

104 only $\Gamma_s \subset \partial\Omega$ is of interest and will be modified, any other boundary will be
 105 fixed during the iterations.

106 We want to find $\partial\Omega$ such that the displacement of the model $u(\Omega)$ is as
 107 close as possible to the observed displacement u_o on the surface Γ_u . Thus,
 108 the unconstrained shape optimization problem we want to solve is the mini-
 109 mization of a squared RMS discrepancy

$$\min_{\Omega} J(\Omega) = \int_{\Gamma_u} (u(\Omega) - u_o)^2 dS \quad (1)$$

110 2.2 Hadamard Boundary Variation

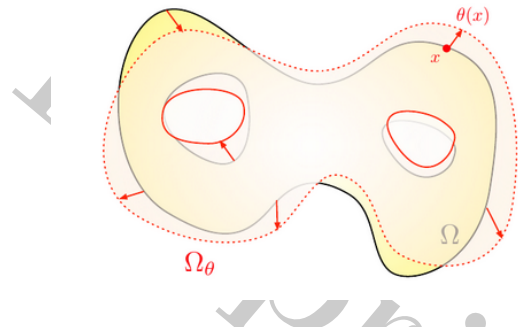


Figure 2: Reproduced from Allaire et al., 2021

111 Overall, this method can be considered a classical iterative gradient de-
 112 scent algorithm. J is first initialized at J_0 with an instructed first guess for
 113 Ω_0 and then iteratively decreased by moving $\partial\Omega$ of a given step in a given
 114 descent direction $\theta : \mathbb{R}^3 \mapsto \mathbb{R}^3 \in W^{1,\inf}$ (the Sobolev space of uniformly
 115 bounded functions, Allaire et al., 2021) chosen using the shape derivative
 116 $J'(\Omega)(\theta)$.

117 The boundary variation method of Hadamard, 1908 introduces the no-
 118 tion of shape differentiation $F'(\Omega)(\theta)$ of a functional F defined on Ω in the
 119 direction θ . In short, such a derivative is based on the variation of a bounded
 120 domain $\Omega \mapsto \Omega_\theta := (Id + \theta)(\Omega)$: the surface $\partial\Omega$ is slightly moved according
 121 to a small vector field $\theta(x)$, as shown in Fig. 2. Once such a derivative
 122 exists, one can compute a descending direction at the n^{th} step θ_n , such as
 123 $J'(\Omega)(\theta_n) \leq 0$, so $J_{n+1} \leq J_n$, to decrease the value of J at each iteration.

124 In our case, after derivation based on the Cea, 1986 formal method, we
 125 found under the variational form :

$$J'(\Omega)(\theta) = \int_{\Gamma_s} \left(Ae(u) : e(p) + \frac{\partial f_s}{\partial n} p + \frac{\partial p}{\partial n} f_s + \kappa f_s p \right) \cdot \theta \cdot n dS \quad (2)$$

126 where $\kappa = \operatorname{div}(n)$ is the mean curvature at the boundary, and p is the
127 adjoint solution of

$$\forall v \in H^1(\mathbb{R}^3), \int_{\Gamma_u} 2(u_\Omega - u_o)v dS + \int_{\Omega} Ae(v) : e(p) dV = 0 \quad (3)$$

and $p = 0$ on Γ_b

128 From there, we can trivially move Ω in the direction $\theta = -A$ (where
129 A is the integrand term in parentheses) to ensure that $J'(\Omega)(\theta) \leq 0$. This
130 guarantees that $J(\Omega_{n+1}) \leq J(\Omega_n)$: the series $J(\Omega_n)$ converges to a minimum.

131 2.3 Level-set representation

132 A key issue is the representation of the surface to be optimized. The level
133 set method allows to track dramatic changes as well as topology variations
134 (creation of new holes). A certain function $\phi : D \mapsto \mathbb{R}$ is defined over the
135 domain $D \in \mathbb{R}^3$ in such a way that the shape boundary is the level set 0,
136 i.e. reads $\partial\Omega = \phi(x = 0)$. Basically, ϕ can be taken as the signed distance
137 between any point x and $\partial\Omega$, as shown in the example fig. 3. In this way,
138 $\partial\Omega$ is implicitly manipulated when transforming ϕ .

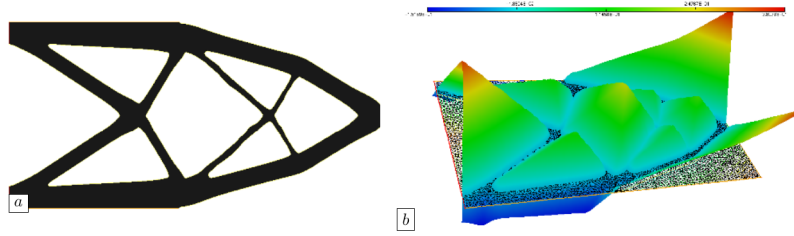


Figure 3: Reproduced from Dapogny and Feppon, 2023

139 Ω_n is then deformed by advecting the corresponding ϕ_n with a velocity
140 field $V(x) = \tau_n \theta_n$, where τ_n is the additional step size. The advection equa-
141 tion usually appears in fluid mechanics to describe the evolution of a quantity
142 transported by a given velocity field, but here there is a smooth and flexible
143 way to modify ϕ which ensures smoothness of Ω_{n+1} and change of topology
144 (see Allaire et al., 2021).

145 2.4 Numerical implementation

146 In practice, the D domain is discretized into a mesh T_n on which each vari-
147 ational form is solved at each iteration n . This includes the solution of the

148 elasticity to get u_n , the adjoint state p_n , the computation of the shape gradient J'_n , the descent direction θ_n , the advection of ϕ_n . In **sotuto** it is achieved
149 by calling scripts written in FreeFem++, a finite element software that allows
150 solving any integral form of elliptic PDE (Hecht, 2012).
151

152 Once the new form Ω_{n+1} is computed and discretized thanks to a local
153 remeshing phase, a new evaluation of J^{n+1} is performed. Since τ is arbitrarily
154 fixed and initialized to 1, it can happen that Ω_n is shifted by too large a step
155 and so $J_{n+1} \geq J_n$. To adjust the step size, a line search procedure is
156 implemented and adjusts the step size by decreasing it if the new iteration
157 is the worst to ensure an improvement of J by computing a new Ω_{n+1} being
158 a less deformed version of Ω_n . On the contrary, if Ω_{n+1} is accepted, τ is
159 increased to speed up convergence. A tolerance is set to accept iterations if
160 the increase in J is reasonable.

161 The global optimization loop has no termination criterion. Thus, it is up
162 to the user to stop it when no significant improvement in J can be achieved,
163 or when the shape is not realistic.

164 The loop and the line search are implemented in Python in **sotuto**. Then
165 the FreeFem scripts are called by the Python script core and data is ex-
166 changed via temporary files.

167 The above aspects are implemented in **sotuto**. However, we extended its
168 functionality to handle our geophysical problem, in a fork we called **magmaOpt**.
169 This included: scripts to create the domain and initial source with a flexible
170 mesher GMSH which handle complex geometries such as the one generated
171 by topography Geuzaine et al., 2009 ,adapting FreeFem scripts to different
172 error functions, allowing optimization of the loaded boundary Γ_s and so on.

173 3 Validation with synthetic data

174 To test the method, the idea is to do a kind of cross-validation. On the
175 one hand, we form synthetic observation data from a known source. On
176 the other hand, we initialized the algorithm with a first guess for the source
177 shape and location. We expect the algorithm to iteratively modify the shape
178 of the source and converge to the correct shape and location. In fact, the
179 3D location of the source (e.g., its center of gravity for a random shape) is
180 not directly optimized as a vector of discrete parameters, but is modified by
181 the simple fact that the boundary is free to move in any direction, and thus
182 can take on a kind of "average rigid body motion" as it gradually moves the
183 center in a given direction.

184 In practice, the synthetic observed surface displacement field is derived
185 from the McTigue, 1987 solution, an analytical approximation of the dis-

placement caused by a uniformly pressurized spherical cavity (the magma domain) embedded in an isotropic, homogeneous, and planar elastic medium (the host crust) with elastic constants t_p $E = 10\text{GPa}$ and $\mu = 0.25$.

Usually, the quantities to be determined with parametric inversion based on a McTigue model are the location and the radius. The pressure change can also be left as a free parameter, but is interchangeable with the radius, so one must be fixed to determine the other, see (Greiner, 2021) for more details. For the synthetic source, we fixed these free parameters to $z = -5\text{km}$, $\Delta P = 10\text{MPa}$, $R = 1.5\text{km}$, which are typical values for inverted magmatic domains.

`magmaOpt` is then allowed to run freely, without any termination condition, to see whether or not it succeeds in converging from the ellipsoid to the McTigue sphere we used to generate the synthetic displacement.

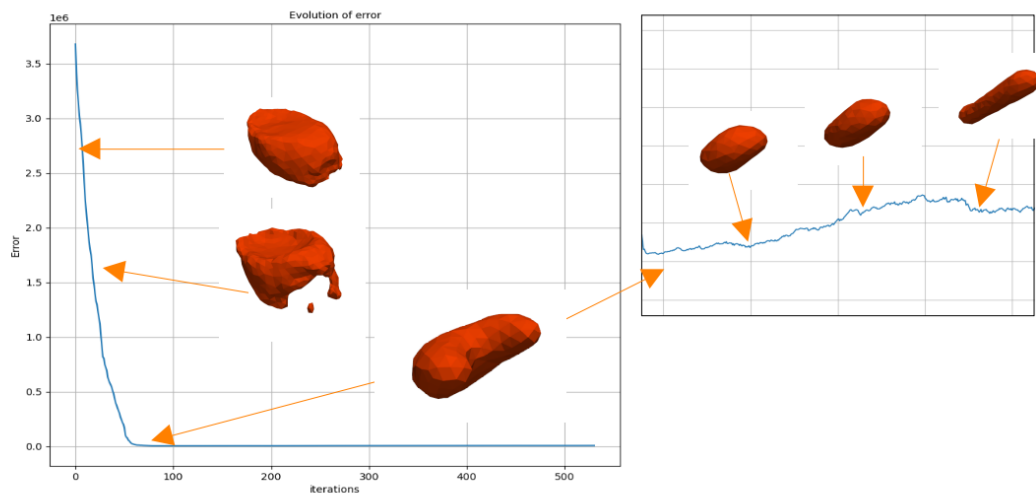


Figure 4: Evolution of error and successive shapes taken by the magma source during an optimization loop. The initial guess is a flat ellipsoid of semi-axes $r_x = 2\text{km}$, $r_y = 3\text{km}$, $r_z = 1\text{km}$ centered on the true spherical source. The minimum is reached at iteration 82.

As shown in the figure 4, the algorithm seems to converge to a minimum. After that, the slope of the cost function is positive because a small increase in J is allowed. It is obvious that no other minima are found, as the shape evolves towards a stick-shaped feature, far from the expected solution. We can also discuss the minima found. The surface reached is obviously not a sphere, but it is closer than any shape found before. We expect the shape to

205 be closer to a sphere with a finer mesh defined. Many improvements could be
 206 realized: for example, once it is obvious that the algorithm will not converge
 207 to a better solution, we could restart the algorithm on the best solution
 208 found, set new evolution parameters, and allow a finer mesh. By repeating
 209 this process automatically, it may be possible to arrive at a more likely shape
 210 for the magma reservoir.

211 4 Real test case : Svartsengi 2022 inflation

212 We now apply the method to infer the shape of a magma domain in a recent
 213 period of volcanic unrest and eruption in SW Iceland by evaluating the shape
 214 of a magma body responsible for the ground inflation observed from 21 April
 215 to 14 June 2022 at Svartsengi on the Reykjanes peninsula. This is one of
 216 5 inflation episodes that preceded catastrophic dike breaches and eruptions
 217 at the Sundhnúkur crater row, which caused the destruction of the city of
 218 Grindavík (Sigmundsson et al., 2024).

219 The observational data used are the line-of-sight (LOS) displacement
 220 maps of the area from Cosmo SkyMed available in Parks et al., 2024, the
 221 data used in Sigmundsson et al., 2024. After uniform downsampling and
 222 mesh reprojection (the data points must be aligned on the mesh nodes), the
 223 ascending A32 and descending D132 tracks were both used in the RMS error
 224 function we adapted to the LOS geometry.

$$J(\Omega) = \sum_{i \in tck} \alpha_i \int_{\Gamma_u} (L_i(u(x)) - l_o^i(x))^2 dS \quad (4)$$

225 Where $tck = \{A125, D132\}$. For each track i , α_i is the weight of the track
 226 ($\forall i, \alpha_i = 1$ here), $L_i : \mathbb{R}^3 \mapsto \mathbb{R}$ is the function that projects the 3D sur-
 227 face displacement given by the model into the LOS geometry, and l_o^i is the
 228 observed LOS displacement.

229 We then used the framework developed above, only projecting the InSAR
 230 data onto the mesh of D and modifying the expression of the error function
 231 in `magmaOpt`.

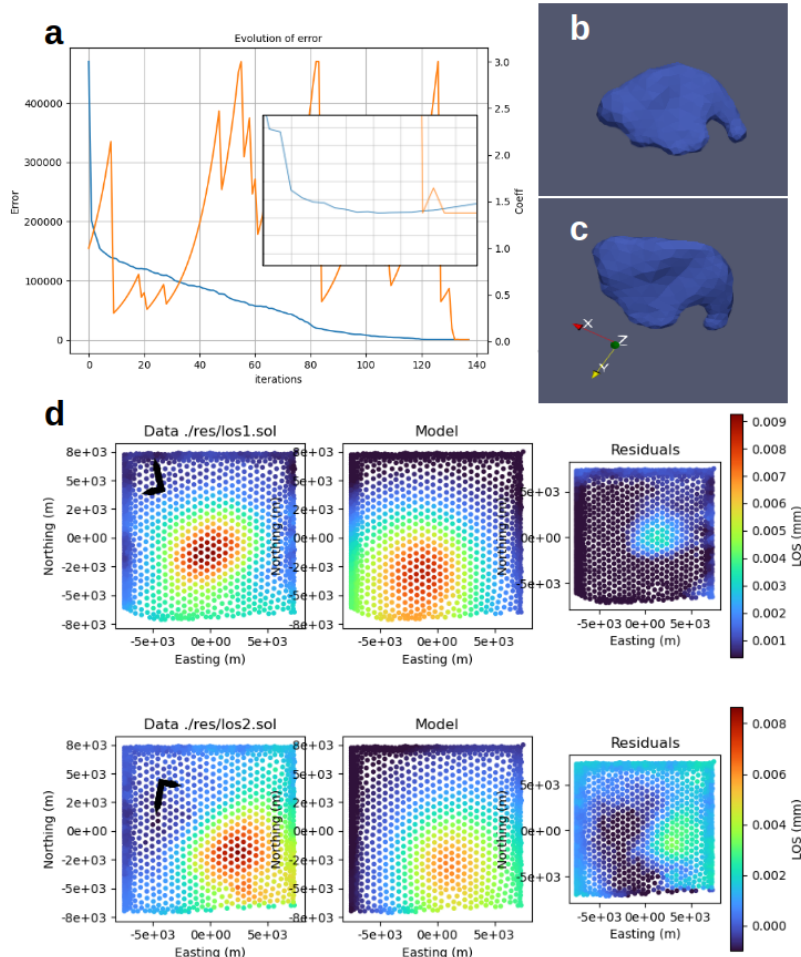


Figure 5: a) Convergence plot with embedded zoom. The blue line is the error and the orange line is the evolution of τ . Minima are reached at iteration 128. b,c) Side and top view of the source Γ_s minimizing J . d) Data, model and residuals of the LOS displacements at iteration 128 for the two InSAR tracks A32 (top) and D132 (bottom). Black arrows are heading and looking directions, coordinates are ISN16 **islands** shifted to a local origin (2529373E, 179745N).

232 The results shown in figure 5 are encouraging: after providing an initial
 233 guess located at the center of inflation at depth for a sphere of radius RR,
 234 the algorithm is able to iteratively change the shape and depth of the magma
 235 domain to finally result in a sill-like flattened spheroid whose centroid is lo-
 236 cated at DD depth. This is consistent with the presumed depth found in
 237 the supporting information of Sigmundsson et al., 2024, which performs an

238 analytical model-based inversion. Although the pressure must be fixed, as
239 explained in 1.2, the result can be used to compare the final shape of the
240 magmatic intrusion and give a richer insight into it. Here we see interesting
241 features, such as an increasing thickness on the north side, that can't
242 be traced by any other method. The algorithm produces features that we
243 consider to be artifacts, probably due to mesh refinement problems, such as
244 small holes or horn-shaped features.

245 5 Discussion

246 This work paves the way for a new class of methods that tackle an unknown
247 geometry of the magmatic domains, thus giving the possibility to explore
248 irregular shapes that are more likely to exist compared to any other usually
249 assumed regular shapes. However, even if the first results presented are
250 promising, many questions remain to be answered. First of all, the internal
251 pressure of the chamber must be specified, which is a strong hypothesis.
252 In this context, the precise shape of the source should be determined as a
253 second step. The traditional analytical model-based inversion would be run
254 first, giving a pressure and a first educated guess for the position and shape
255 of Ω_0 . Then a more realistic shape could be sought with a shape optimization
256 taking the output of the inversion as an initial guess.

257 Adding constraints may also be an interesting way to explore. For ex-
258 ample, the volume of the source could be constrained to be within bounds
259 or even to match a certain value. The implemented shape optimization is
260 certainly able to handle constraints as described by [allaire202](#). The physical
261 meaning of the best shape might benefit from a more constrained problem,
262 and the less influencing deeper part of the source might be less random.

263 To better understand the influence of data partitioning and variablitiy,
264 additional tests could be run with synthetic data. We can think of tests
265 such as masking part of the surface displacement field, introducing noise
266 and parasitic signals, reducing the number of data points, as is often the
267 case in reality with areas of volcanic systems lacking data coverage (glacier,
268 river, lava, forest) and subjected to perturbations (atmospheric distortion,
269 weather).

270 It is also important to mention that the behavior of the algorithm is
271 influenced by numerous parameters of varying importance, starting from the
272 discretization length (element size) or the domain extent, to the limits of the
273 step size τ , the regularization length, or the number of iterations allowed by
274 the line search. A systematic study of each of these parameters would be
275 beneficial in assessing the quality of the shape inferred.

276 Exploring a way to quantify the uncertainty of the answer is also crucial.
277 For example, a sensitivity analysis approach could be considered, as well as
278 the inclusion of a probabilistic quantity.

279 6 Conclusion

280 The present study has successfully demonstrated the application of inverse
281 problems and computational methods to infer the shape of a magma domain
282 beneath a volcano using ground inflation data from satellite observations.
283 The shape optimization technique used in this research showed a new way to
284 identify the most likely shape of the magma chamber. It was intended as an
285 opening to new methods rather than a complete solution.

286 We have shown that modifying a shape optimization algorithm to handle
287 geophysical problems is feasible and of interest. Tests on synthetic data
288 showed to some extent the relevance of the approach, although the best
289 sources found exposed the limitations faced by these first attempts of shape
290 optimization for volcano geodesy. The test on real data showed a concrete
291 case of how the method could be used after being more mature.

292 The perspectives are numerous. The numerical nature of the models
293 allows to easily add complexities to the modeling, such as complex mechanical
294 behavior of the crust (plaxticity, viscoelasticity, poroelsaticity), additional
295 loads (tectonic stress, tidal loads, glacier weights), or inhomogeneities. We
296 hope that the open source code `magmaOpt` developed by us will be modified
297 and extended by future work.

298 By addressing these limitations and extending this approach, researchers
299 can further improve the accuracy and reliability of magma domain shape
300 inference. Ultimately, the development of more sophisticated models will
301 enable geophysicists to better monitor volcanic activity, predict eruptions,
302 and provide critical support for hazard mitigation strategies.

303 References

- 304 Allaire, G., Dapogny, C., & Jouve, F. (2021). Chapter 1 - Shape and topology
305 optimization. In A. Bonito & R. H. Nochetto (Eds.), *Geometric partial
306 differential equations - part II* (pp. 1–132). Elsevier. <https://doi.org/10.1016/bs.hna.2020.10.004>
307

- 308 Andreassen, E., Clausen, A., Schevenels, M., Lazarov, B. S., & Sigmund, O.
309 (2011). Efficient topology optimization in MATLAB using 88 lines
310 of code. *Structural and Multidisciplinary Optimization*, 43(1), 1–16.
311 <https://doi.org/10.1007/s00158-010-0594-7>
- 312 Bagnardi, M., & Hooper, A. (2018). Inversion of Surface Deformation Data
313 for Rapid Estimates of Source Parameters and Uncertainties: A Bayesian
314 Approach. *Geochemistry, Geophysics, Geosystems*, 19(7), 2194–2211.
315 <https://doi.org/10.1029/2018GC007585>
- 316 Beghini, L. L., Beghini, A., Katz, N., Baker, W. F., & Paulino, G. H. (2014).
317 Connecting architecture and engineering through structural topology
318 optimization. *Engineering Structures*, 59, 716–726. <https://doi.org/10.1016/j.engstruct.2013.10.032>
- 319 320 Bendsøe, M. P., & Sigmund, O. (2004). Topology optimization by distribu-
321 tion of isotropic material. In M. P. Bendsøe & O. Sigmund (Eds.),
322 *Topology Optimization: Theory, Methods, and Applications* (pp. 1–
323 69). Springer. https://doi.org/10.1007/978-3-662-05086-6_1
- 324 Cea, J. (1986). Conception optimale ou identification de formes, calcul rapide
325 de la dérivée directionnelle de la fonction coût. *ESAIM: Modélisation
326 mathématique et analyse numérique*, 20(3), 371–402. Retrieved Au-
327 gust 22, 2024, from http://www.numdam.org/item/M2AN_1986_20_3_371_0/
- 328 329 Cervelli, P., Murray, M. H., Segall, P., Aoki, Y., & Kato, T. (2001). Estimat-
330 ing source parameters from deformation data, with an application
331 to the March 1997 earthquake swarm off the Izu Peninsula, Japan.
332 *Journal of Geophysical Research: Solid Earth*, 106(B6), 11217–11237.
333 <https://doi.org/10.1029/2000JB900399>
- 334 Charco, M., & Galán del Sastre, P. (2014). Efficient inversion of three-
335 dimensional finite element models of volcano deformation. *Geophysical
336 Journal International*, 196(3), 1441–1454. <https://doi.org/10.1093/gji/gjt490>
- 337 338 Dapogny, C., & Bonnetier, E. (n.d.). *An introduction to shape and topology
339 optimization*. Retrieved August 21, 2024, from <https://membres-ljk.imag.fr/Charles.Dapogny/coursoptim.html>
- 340 341 Dapogny, C., & Feppon, F. (2023). Shape optimization using a level set based
342 mesh evolution method: An overview and tutorial. *Comptes Rendus.
343 Mathématique*, 361(G8), 1267–1332. <https://doi.org/10.5802/crmath.498>
- 344 345 Dapogny, C., & Feppon, F. (2024, July 30). *Dapogny/sotuto*. Retrieved Au-
346 gust 21, 2024, from <https://github.com/dapogny/sotuto>

- 347 Dzurisin, D. (2007). *Volcano deformation: Geodetic monitoring techniques*.
 348 Springer ; Praxis
 349 OCLC: ocm61180785.
- 350 Feppon, F., Allaire, G., Dapogny, C., & Jolivet, P. (2020). Topology optimization of thermal fluid–structure systems using body-fitted meshes and parallel computing. *Journal of Computational Physics*, 417, 109574. <https://doi.org/10.1016/j.jcp.2020.109574>
- 354 Frei, W. (2015, December 29). *Designing New Structures with Shape Optimization*. COMSOL. Retrieved August 22, 2024, from <https://www.comsol.com/blogs/designing-new-structures-with-shape-optimization>
- 358 Geuzaine, C., Remacle, J.-F., & Dular, P. (2009). Gmsh: A three-dimensional finite element mesh generator. *International Journal for Numerical Methods in Engineering*, 79(11), 1309–1331.
- 361 Greiner, S. H. (2021). *Including topography and a 3D-elastic structure into a Finite-Element deformation model of Grímsvötn, Iceland* (Doctoral dissertation). <http://hdl.handle.net/1946/38435>
- 364 Hadamard, J. (1908). *Mémoire sur le problème d'analyse relatif à l'équilibre des plaques élastiques encastrées*. Imprimerie nationale. <https://books.google.co.ma/books?id=8wSUmAEACAAJ>
- 367 Hecht, F. (2012). New development in FreeFem++. *Journal of Numerical Mathematics*, 20(3-4), 251–265. <https://freefem.org/>
- 369 Hickey, J., & Gottsmann, J. (2014). Benchmarking and developing numerical Finite Element models of volcanic deformation. *Journal of Volcanology and Geothermal Research*, 280, 126–130. <https://doi.org/10.1016/j.jvolgeores.2014.05.011>
- 373 Hunter, W., et al. (2017). ToPy - topology optimization with python. *Github*. <https://github.com/williamhunter/topy>
- 375 Le Quilliec, G. (2014). Topology optimization procedure TOPOPTIM and other various developments made with Cast3M. <https://doi.org/10.13140/2.1.2718.3682>
- 378 McTigue, D. F. (1987). Elastic stress and deformation near a finite spherical magma body: Resolution of the point source paradox. *Journal of Geophysical Research: Solid Earth*, 92(B12), 12931–12940. <https://doi.org/10.1029/JB092iB12p12931>
- 382 Mogi, K. (1958). Relations between the eruptions of various volcanoes and the deformations of the ground surfaces around them. *Earthq Res Inst*, 36, 99–134.
- 385 Parks, M., Drouin, V., Geirsson, H., Hooper, A., Hreinsdóttir, S., Ófeigsson, B., Friðriksdóttir, H. M., Vogfjörd, K. S., Lanzi, C., & Tolpekin, V. (2024). Data and geodetic modelling results for Science article "Frac-

- 388 turing and tectonic stress drives ultra-rapid magma flow into dikes".
389 Retrieved August 21, 2024, from <https://osf.io/9rcq7/>
- 390 Sigmund, O. (2001). A 99 line topology optimization code written in Matlab.
391 *Structural and Multidisciplinary Optimization*, 21(2), 120–127. <https://doi.org/10.1007/s001580050176>
- 392 Sigmund, O., & Maute, K. (2013). Topology optimization approaches. *Structural and Multidisciplinary Optimization*, 48(6), 1031–1055. <https://doi.org/10.1007/s00158-013-0978-6>
- 393 Sigmundsson, F., Parks, M., Geirsson, H., Hooper, A., Drouin, V., Vogfjörd,
394 K. S., Ófeigsson, B. G., Greiner, S. H. M., Yang, Y., Lanzi, C., De Pas-
395 cale, G. P., Jónsdóttir, K., Hreinsdóttir, S., Tolpekin, V., Friðrikssdóttir,
396 H. M., Einarsson, P., & Barsotti, S. (2024). Fracturing and tectonic
397 stress drive ultrarapid magma flow into dikes. *Science*, 383(6688),
398 1228–1235. <https://doi.org/10.1126/science.adn2838>
- 399 Slavov, S., & Konsulova-Bakalova, M. (2019). Optimizing Weight of Housing
400 Elements of Two-stage Reducer by Using the Topology Management
401 Optimization Capabilities Integrated in SOLIDWORKS: A Case
402 Study. *Machines*, 7(1), 9. <https://doi.org/10.3390/machines7010009>
- 403 Taylor, N. C., Johnson, J. H., & Herd, R. A. (2021). Making the most of the
404 Mogi model: Size matters. *Journal of Volcanology and Geothermal
405 Research*, 419, 107380. <https://doi.org/10.1016/j.jvolgeores.2021.107380>
- 406 Trasatti, E. (2022). Volcanic and Seismic Source Modeling: An Open Tool
407 for Geodetic Data Modeling. *Frontiers in Earth Science*, 10. <https://doi.org/10.3389/feart.2022.917222>
- 408 Velez, M. L., Euillades, P., Caselli, A., Blanco, M., & Díaz, J. M. (2011).
409 Deformation of Copahue volcano: Inversion of InSAR data using a
410 genetic algorithm. *Journal of Volcanology and Geothermal Research*,
411 202(1), 117–126. <https://doi.org/10.1016/j.jvolgeores.2011.01.012>
- 412 Yang, X.-M., Davis, P. M., & Dieterich, J. H. (1988). Deformation from in-
413 flation of a dipping finite prolate spheroid in an elastic half-space as
414 a model for volcanic stressing. *Journal of Geophysical Research: Solid
415 Earth*, 93(B5), 4249–4257. <https://doi.org/10.1029/JB093iB05p04249>